Sensitivity of Tornado Dynamics to Soil Debris Loading

DAVID J. BODINE,[a,b,c] TAKASHI MARUYAMA,[d] ROBERT D. PALMER,[b,c] CALEB J. FULTON,[c,e] HOWARD B. BLUESTEIN,[b] AND DAVID C. LEWELLEN[f]

[a] *Advanced Study Program, National Center for Atmospheric Research,*[g] *Boulder, Colorado*
[b] *School of Meteorology, University of Oklahoma, Norman, Oklahoma*
[c] *Advanced Radar Research Center, University of Oklahoma, Norman, Oklahoma*
[d] *Disaster Prevention Research Institute, Kyoto University, Kyoto, Japan*
[e] *School of Electrical and Computer Engineering, University of Oklahoma, Norman, Oklahoma*
[f] *Department of Mechanical and Aerospace Engineering, West Virginia University, Morgantown, West Virginia*

(Manuscript received 30 June 2015, in final form 21 March 2016)

ABSTRACT

Past numerical simulation studies found that debris loading from sand-sized particles may substantially affect tornado dynamics, causing reductions in near-surface wind speeds up to 50%. To further examine debris loading effects, simulations are performed using a large-eddy simulation model with a two-way drag force coupling between air and sand. Simulations encompass a large range of surface debris fluxes that cause negligible to substantial impact on tornado dynamics for a high-swirl tornado vortex simulation.

Simulations are considered for a specific case with a single vortex flow type (swirl ratio, intensity, and translation velocity) and a fixed set of debris and aerodynamic parameters. Thus, it is stressed that these findings apply to the specific flow and debris parameters herein and would likely vary for different flows or debris parameters. For this specific case, initial surface debris fluxes are varied over a factor of 16 384, and debris cloud mass varies by only 42% of this range because a negative feedback reduces near-surface horizontal velocities. Debris loading effects on the axisymmetric mean flow are evident when maximum debris loading exceeds 0.1 kg kg^{-1}, but instantaneous maximum wind speed and TKE exhibit small changes at smaller debris loadings (greater than 0.01 kg kg^{-1}). Initially, wind speeds are reduced in a shallow, near-surface layer, but the magnitude and depth of these changes increases with higher debris loading. At high debris loading, near-surface horizontal wind speeds are reduced by 30%–60% in the lowest 10 m AGL. In moderate and high debris loading scenarios, the number and intensity of subvortices also decrease close to the surface.

1. Introduction

Large amounts of lofted debris are often evident from visual or radar observations of tornadoes. Dust or soil clouds with varied widths, heights, and opacities frequently surround the condensation funnel. Tornadoes can also loft larger debris elements, possibly anthropogenic in origin. While dust and soil particles are small and remain lofted around the tornado, larger debris elements acquire greater radial velocities because of large centrifugal forces and are typically centrifuged at a lower altitude (Dowell et al. 2005). Debris lofted by tornadoes produces a unique polarimetric radar signature called the tornadic debris signature (TDS; Ryzhkov et al. 2002, 2005). TDS statistics vary substantially among tornadoes and within individual tornado events (Ryzhkov et al. 2005; Schultz et al. 2012; Bodine et al. 2013; Van Den Broeke and Jauernic 2014), suggesting large variations in the amount and/or type of debris lofted.

Debris loading effects of sand-sized particles on tornado dynamics were first studied by Lewellen et al. (2004), Gong (2006), and Lewellen et al. (2008) using a large-eddy simulation (LES) model. Lewellen et al. (2008) found that debris loading D_L, defined as the ratio of the mass of debris to the mass of air, could exceed 1 kg kg^{-1} in the corner flow region, causing substantial

[g] The National Center for Atmospheric Research is sponsored by the National Science Foundation.

Corresponding author address: David Bodine, Advanced Study Program, National Center for Atmospheric Research, 3450 Mitchell Lane, Boulder, CO 80302.
E-mail: dbodine@ucar.edu

DOI: 10.1175/JAS-D-15-0188.1

© 2016 American Meteorological Society

momentum exchange between air and sand particles. In these simulations, maximum azimuthal velocities are reduced by 20%–50%, and subvortices are weakened or eliminated. Since tornado dynamics are sensitive to changes in corner flow dynamics (Lewellen et al. 2000; Lewellen and Lewellen 2007a,b), wind speed changes aloft occur even in regions with small air–debris momentum exchange. Lewellen et al. (2008) found that reduced near-surface azimuthal wind speeds change radial and vertical pressure gradients, thereby impacting tornado dynamics outside of high debris loading regions.

Surface debris fluxes are likely affected by both surface and flow characteristics and thus likely vary between tornadoes and even along a tornado's path. Differences in surface characteristics, such as vegetation cover, soil adhesion, or surface roughness, would likely cause different soil surface fluxes for two tornadoes with identical kinematic characteristics. A simple example is that loose soil with no vegetation cover would be easier to erode than compacted soil with vegetation cover. Thus, the bare, loose soil would produce higher surface fluxes.

A significant challenge to modeling tornado debris loading effects is that soil debris fluxes in tornadoes have not been measured. So the most relevant measurements are laboratory and dust devil soil flux measurements. Wind tunnel studies can test the relationship between wind speed and soil fluxes in a controlled environment and have been conducted for high-speed flows (Batt et al. 1999). Lewellen et al. (2008) used data from Batt et al.'s (1999) study to determine soil fluxes in their debris loading simulations. Neakrase and Greeley (2010) performed laboratory experiments with vortices similar to dust devils to examine the impact of surface roughness on surface fluxes and found that surface fluxes varied over several orders of magnitude (10^{-5} to $1\,\mathrm{kg\,m^{-2}\,s^{-1}}$). In situ measurements of soil fluxes in dust devils have been made (Metzger et al. 2011) and found fluxes in the lower portion of the surface fluxes measured by Neakrase and Greeley (2010). Although these studies were conducted for dust devils and similar laboratory vortices, they suggest that a large range of surface fluxes may occur over different surface types.

The goal of this study is to examine the sensitivity of tornado dynamics to surface debris fluxes and associated debris loadings. Surface debris fluxes are varied over several orders of magnitude in an LES model with a realistic soil particle-size distribution. Given the inherent complexities of relating soil fluxes as a function of wind speed to different surface types, the goal of this study is not to examine a specific surface type but to quantify and assess how tornado dynamics respond to different debris fluxes. The range of tested fluxes could reflect different surface characteristics encountered by tornadoes as well as the uncertainties in surface debris fluxes that occur in tornadoes. Since surface debris fluxes in tornadoes have not been measured, it should be noted that some tested surface debris fluxes might not occur in nature and that larger or smaller surface debris fluxes outside of the tested range could also occur. Nonetheless, the study aims to test surface debris fluxes that encompass a large range of possible effects on tornado dynamics and determine when debris loading effects become important for the specific case presented.

The simulations herein focus on a specific case with a high-swirl vortex flow with no translation velocity and a single parameterization for surface debris and aerodynamic properties [e.g., soil particle-size distribution (PSD) and power-law relationship between wind speed and surface debris fluxes]. It is emphasized that the forthcoming analysis and conclusions apply to this specific case, and different debris or flow characteristics would likely produce different debris loading effects on tornado dynamics. In reality, these parameters vary between tornadoes and probably within a single tornado case. Thus, a larger range of flow, debris, and aerodynamic parameters should be tested, but that is beyond the scope of this study.

This study is organized in the following manner: In section 2, the LES model and drag force feedback model are described. Sensitivity tests are performed to examine debris loading effects on tornado dynamics in section 3. Conclusions are summarized and discussed in section 4.

2. LES model description and drag force feedback model

a. *LES model*

The present study makes use of an LES model to examine the sensitivity of tornado dynamics to debris loading. The LES model is based on the Research Institute for Applied Mechanics Computational Prediction of Airflow over Complex Terrain (RIAM-COMPACT) model at Kyushu University (Uchida and Ohya 2003). Maruyama (2011) discusses modifications of the LES model for tornado simulations and debris trajectory calculations for spherical debris. In this study, the LES model is configured with 175, 175, and 79 grid points in the x, y, and z dimensions, respectively, and the horizontal and vertical dimensions of the model domain (l_{dom} and h_{dom}) are 1 and 1.8 km, respectively, similar to past LES studies of tornadoes (e.g., Lewellen et al. 1997). A stretched grid is used throughout the domain to provide maximum resolution near the surface and vortex center. Horizontal grid spacing is stretched from the center of the domain and varies from 2.8 to 16.8 m, while the vertical grid spacing is stretched from the surface and varies from

2.8 to 98 m. The maximum change in grid spacing between adjacent horizontal and vertical points is 7% and 9%, respectively. Within the radius of maximum wind (about 200 m), the horizontal grid is stretched more slowly between 2.8 and 4.5 m. Although the 2.8-m minimum resolution resolves finer-scale flow structures, such as subvortices, it is cautioned that simulations with higher grid resolution would better resolve the detailed wind and debris loading characteristics associated with subvortices (described in section 3c).

The horizontal and vertical boundary conditions (BCs) of the LES model produce a high-swirl flow with subvortices. The horizontal boundary conditions of the LES model impose an approximately axisymmetric flow through an inflow layer depth of 200 m. On the horizontal boundaries, a logarithmic wind profile is specified with a roughness length z_0 of 0.01 m. On the lower BC, a logarithmic wind profile is specified by computing the first gridpoint surface stress based on (1) and (2), where u_* is the friction velocity, V_H is the horizontal wind speed, and κ is Von Kármán's constant:

$$u_* = V_H(z_1)\kappa \Big/ \log\left(\frac{z_1}{z_0}\right); \quad \text{and} \tag{1}$$

$$\tau = \rho u_*^2 . \tag{2}$$

Surface stresses are then divided into x and y components. Above the specified inflow layer depth, inflow velocities are $0\,\mathrm{m\,s^{-1}}$, while angular momentum is held constant. Vertical velocities on the top BC specify a central downdraft surrounded by an annulus of updraft as follows:

$$w(r) = \begin{cases} 44.8\dfrac{r}{0.4l_{\mathrm{dom}}} - 20 & r \le 0.4l_{\mathrm{dom}} \\ 24.8 & r > 0.4l_{\mathrm{dom}} \end{cases}. \tag{3}$$

The top BC conditions produce a mean updraft of $19\,\mathrm{m\,s^{-1}}$ within a 0.5-km radius from the center of the domain. The updraft drives an inward, swirling flow in the lowest 200 m with a mean angular momentum Γ of $11\,600\,\mathrm{m^2\,s^{-1}}$ at a 500-m radius. The horizontal and top BCs (representing a larger-scale updraft) are held constant during the simulation. Thus, the impact of debris loading on the larger-scale circulation is not incorporated but could lead to additional feedbacks (e.g., through negative buoyancy effects).

b. *Debris trajectory calculation and two-way drag force model*

The implementation of tornadic debris in the LES model herein differs from the "two-fluid" approach used by Gong (2006) and Lewellen et al. (2008) in that Lagrangian debris trajectories are calculated and a body force term is added to the filtered Navier–Stokes equations to model two-way air–debris coupling. A potential advantage of the Lagrangian approach is that a large number of trajectories are provided within the tornado-like vortex, allowing for variability of debris velocity in each grid cell. The disadvantage to the trajectory-based approach is that the number of trajectories is limited by computational resources; in this study, the number of trajectories in a particular simulation is limited herein to the order of 10^6 for each particle size.

Debris trajectories are calculated for particle number n using the following equation:

$$\frac{du_{di,n}}{dt} = \frac{1}{2}\frac{\rho C_D A_n}{m_n}(u_i - u_{di,n})|u_i - u_{di,n}| - g\delta_{i,3}, \tag{4}$$

where ρ is air density, C_D is the drag force coefficient, A_n is debris area, m_n is debris mass, u_i and $u_{di,n}$ are the air and debris velocities (i = 1, 2, and 3 represent the x, y, and z directions), respectively, and g is gravitational acceleration. Debris elements considered herein are approximately spherical and thus are assumed to have isotropic drag coefficients. However, spherical particles still exhibit variations in drag coefficients as a function of particle Reynolds number Re_p:

$$\mathrm{Re}_p = \frac{\rho d_n |u_i - u_{di,n}|}{\mu}, \tag{5}$$

where d_n is debris diameter and μ is air viscosity. To account for the Reynolds number dependence of the drag coefficient, C_D is calculated using an empirical formula from White (1991), as follows:

$$C_D \approx \frac{24}{\mathrm{Re}_p} + \frac{6}{1 + \sqrt{\mathrm{Re}_p}} + 0.4. \tag{6}$$

Using (4)–(6), debris trajectories are calculated using second-order Runge–Kutta integration with a time step of 0.01 s.

Debris trajectories are computed for soil particle radii of 0.1, 0.25, 0.5, 0.75, and 1 mm with a debris density ρ_d of $2650\,\mathrm{kg\,m^{-3}}$. For the 0.1- and 0.25-mm-radii particles, 4 million trajectories are computed; 1 million trajectories are computed for 0.5–1-mm-radius particles. Each trajectory is reinitialized at the surface after exiting the domain. Thus, a greater number of small particle trajectories are used because the small particles have longer residency times within the domain. Sand particles are given a random initial vertical velocity w_{d0} between $\sqrt{2gd}$ and $5u_*$, based on Anderson and Haff (1991),

where u_* is the friction velocity. Huang et al. (2008) used this vertical velocity initialization for sand particles in their LES model. Initial horizontal velocities for sand particles are $0\,\mathrm{m\,s^{-1}}$.

Surface soil fluxes are specified based on a soil particle-size distribution and power-law wind speed relationship. Soil PSDs from geological and agricultural studies (Tyler and Wheatcraft 1989, 1992) are used to specify more realistic PSDs by distributing the mass flux across the five particle sizes. Soil PSDs follow fractal behavior (Turcotte 1986), which allows soil PSDs to be expressed by the following empirical equation:

$$N_s r_s^p = \text{const.}, \tag{7}$$

where N_s is the number of soil particles greater than radius r_s. For sandy and clay loam soils (Tyler and Wheatcraft 1992), p is 2.646 and 2.832, respectively. For a truncated sandy loam PSD using five radii—0.1, 0.25, 0.5, 0.75, and 1 mm—the mass fraction w_l of each particle radius in this PSD is given in Table 1. These are likely common soil types in the Great Plains region, but a broader examination of soil PSDs is needed. Hereafter, we will refer to the soil particles as sand. It is important to note that soil PSDs are only specified at the surface, and differences in soil particle trajectories can produce different soil PSDs aloft (e.g., as a consequence of debris centrifuging).

Surface soil fluxes are modeled based on a power-law wind relationship. Lewellen et al. (2008) assumed sand debris flux increased proportionally to turbulent kinetic energy (TKE) based on straight-line wind tunnel measurements of sand particle fluxes by Batt et al. (1999). Since the current model configuration does not include a prognostic equation for TKE, we assume that upward surface mass flux $M_3^l(k)$ for each particle size l is proportional to horizontal velocity $v_H(k)$ in grid cell k raised to the 3/2 power, as follows:

$$M_3^l(k) = w_l c_f v_H^{3/2}(k), \tag{8}$$

where c_f is a coefficient for the surface debris flux. The total surface soil flux $M_3^{\mathrm{tot}}(k)$ is computed as follows:

$$M_3^{\mathrm{tot}}(k) = \sum_{l=1}^{5} M_3^l(k). \tag{9}$$

To examine the impact of different surface types on tornado dynamics, c_f is tested over a range of several orders of magnitudes. For ease of interpretation, we express c_f as

$$c_f = c_0 \beta, \tag{10}$$

TABLE 1. Representation of a truncated sandy loam PSD, including the particle radii (mm), mass fraction, and example scaling factors for 0.01 kg of soil represented by five trajectories (i.e., the five trajectories represent a total mass of 0.01 kg).

Radius (mm)	w_l	S_n
0.1	0.41	3.735×10^5
0.25	0.23	1.350×10^4
0.5	0.15	1.054×10^3
0.75	0.11	239.6
1	0.09	83.5

where c_0 represents the smallest constant tested in these experiments, and β is the debris flux factor and is varied from 1 to 16384 by powers of 4. Different values of β could represent the effects of different surface characteristics. For example, higher β could represent surfaces from which debris are more easily eroded. Each sensitivity experiment also uses a constant β, and thus it is assumed that debris availability and surface characteristics do not change. Finally, specified horizontal and downward surface debris fluxes are zero (i.e., sand particles falling back to the surface are assumed to stick).

Surface soil fluxes are implemented in the LES model through the following process. Since each soil particle cannot be explicitly represented in the simulation because of computational constraints, a concept called the scaling factor (S_n) is used, where S_n is the number of particles that a trajectory represents. The scaling factor S_n is specified when the trajectory is initialized and is a function of the soil PSD. Example values of S_n are shown for 0.01 kg of sandy loam soil in Table 1. Trajectories for small particles have higher S_n because the radii are smaller and the mass fraction in the soil PSD is larger.

The following equation is used to relate the scaling factor to the surface mass flux [(8)]:

$$S_n = \frac{M_3^l(k)\Delta x_k \Delta y_k t_p(n)}{m_n}, \tag{11}$$

where Δx_k and Δy_k are the widths of grid cell k in the x and y dimensions, respectively, $t_p(n)$ is the time since a trajectory was released from the grid cell, and m_n is a single particle n's mass. That is, this equation calculates the number of soil particles needed to represent the surface mass flux, accounting for how often trajectories become available and model gridcell size differences. In (11), it is evident that higher scaling factors are needed to represent the same surface mass flux for larger grid cells and for slower rates of trajectory initializations. Once the simulation reaches a steady state, t_p has a typical value of 0.05–0.5 s, depending on the rate of trajectory initialization (larger particles have a shorter t_p

as a result of reduced lofting and faster sedimentation). Thus, surface debris fluxes are adjusted at approximately 0.05–0.5 s time resolution for each particle size.

Two-way drag coupling between air and debris is implemented based on Newton's third law. Accordingly, a drag force exerted on a particle requires a reaction force of equal magnitude and opposite direction on the air to conserve momentum. The body force exerted by particle n is given by

$$f_{xi,n} = \frac{1}{2}\rho C_D A_n (u_i - u_{di,n})|u_i - u_{di,n}|. \quad (12)$$

For each grid cell, the body force per unit mass F_{xi} is computed by summing the product of the body forces $f_{xi,n}$ and scaling factors S_n of the N debris trajectories in the grid cell. The subscript n refers to the index of the particles within the grid cell. Then, dividing by ρ and the gridcell volume V_{grid}, F_{xi} is

$$F_{xi} = \frac{1}{\rho V_{\text{grid}}} \sum_{n=1}^{N} S_n f_{xi,n}, \quad (13)$$

where $f_{xi,n}$ is multiplied by S_n to represent S_n particles. To enable two-way drag force coupling, F_{xi} is then subtracted from the spatially averaged Navier–Stokes equation:

$$\frac{\partial \overline{u}_i}{\partial t} + \frac{\partial}{\partial x_j}(\overline{u}_i \overline{u}_j) = -\frac{1}{\rho}\frac{\partial \overline{p}}{\partial x_i} + 2\frac{\partial(\nu + \nu_{\text{SGS}})\overline{D}_{i,j}}{\partial u_i} - F_{xi}, \quad (14)$$

where $\nu = \mu/\rho$ and $\overline{D}_{i,j}$ is

$$\overline{D}_{i,j} = \left(\frac{\partial \overline{u}_j}{\partial \overline{x}_i} + \frac{\partial \overline{u}_i}{\partial \overline{x}_j}\right). \quad (15)$$

Subgrid-scale viscosity ν_{SGS} is modeled using the Smagorinsky turbulence model (Smagorinsky 1963). In the present model configuration, subgrid turbulent mixing effects on debris trajectories and the drag force feedback model are not incorporated.

The primary focus of the study is to examine a large range of initial surface mass fluxes by conducting sensitivity tests with the parameter β and to explore what range of surface mass fluxes affect tornado dynamics. These simulations encompass from negligible to large debris loading effects on tornado dynamics. The debris loading simulations are initialized from a steady-state simulation with no debris, and a control simulation with no debris loading is also conducted. The analysis period for the debris loading experiments focuses on the time period after the tornado debris cloud develops, and the tornado vortex and debris cloud have achieved a steady state.

3. Analysis

Presented in this section are results of sensitivity tests used to assess the impact of variations in surface mass fluxes on a high-swirl tornado simulation. Debris cloud characteristics are examined as a function of surface mass fluxes in section 3a. In section 3b, the axisymmetric spatial structure of time-averaged debris loading and winds is discussed. Then the impact of varied surface mass fluxes on the three-dimensional, time-varying structure of debris loading and winds is analyzed in section 3c. Since the control simulation produces a high-swirl flow with subvortices, the impact of debris loading on subvortices is also examined.

a. Sensitivity of debris cloud characteristics to surface mass fluxes

A negative feedback mechanism is observed over the range of initial surface mass fluxes examined. The initial surface mass flux is determined by lowest gridcell wind speeds at the start of the debris loading simulation (based on the power-law relationship). Since the flow responds to debris loading, time-averaged, steady-state surface debris fluxes differ from this initial value because lowest gridcell velocities are modified by debris loading. In Fig. 1, time-averaged, steady-state statistics are shown for total and lowest grid layer (LGL) debris cloud mass, maximum instantaneous debris loading, and LGL horizontal velocity (raised to the 3/2 power) and surface mass fluxes. For comparison, the initial surface mass flux is shown with the dashed black line. Mean debris cloud mass and maximum debris loading vary from 1.6×10^3 to 11.0×10^7 kg and 6.0×10^{-4} to 7.0 kg kg^{-1}, respectively (Figs. 1a,b). While the range of β and initial surface mass fluxes is varied over a range of 16384, total debris cloud mass increases by only 42%. Lewellen et al. (2008) showed that increasing or decreasing surface mass fluxes by a factor of 2 only caused a change in sand cloud mass of approximately 20% (for a high debris loading simulation). For a case with increasing surface mass fluxes, near-surface wind speeds decrease and reduce the amount of lofted debris, causing a negative feedback. In our simulations, near-surface wind speeds are also reduced, but by a smaller factor. Thus, a smaller negative feedback mechanism occurs. Finally, the LGL contains about 5%–10% of the total debris cloud mass, and larger percentages occur at higher debris loading as a consequence of reduced debris lofting as near-surface vertical velocities decrease (discussed in the next section).

Total debris cloud mass and maximum debris loading become less sensitive to β as β increases. For smaller β and initial surface mass fluxes ($<10^{-2}$ kg m^{-2} s^{-1}), horizontal velocities exhibit little change (Fig. 1c) and

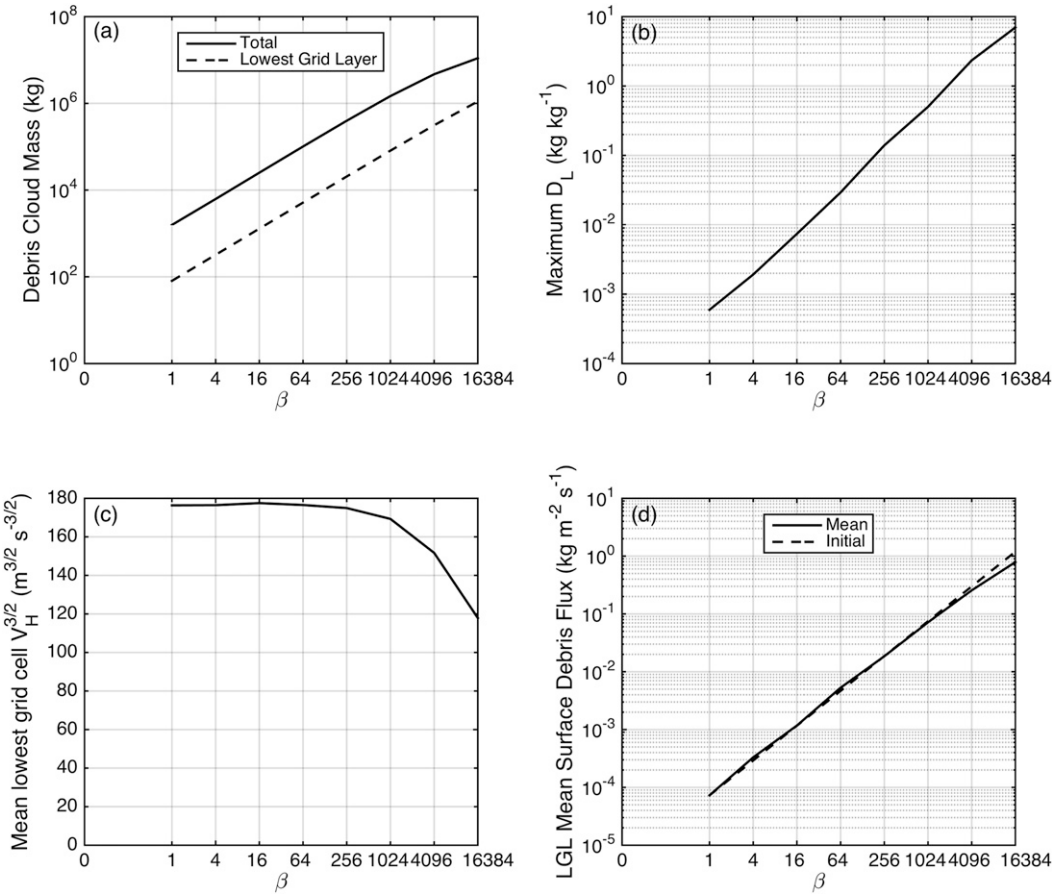

FIG. 1. Time-averaged, steady-state (a) total and LGL debris cloud mass (kg), (b) maximum instantaneous debris loading (kg kg^{-1}), (c) time-averaged, steady-state LGL horizontal velocity, raised to the power of 3/2, and (d) mean surface debris flux (kg m^{-2} s^{-1}) at $t = 0$ s (dashed line) and at a steady state (solid line) in the LGL. Initially, debris cloud mass increases proportional to β. As near-surface fluxes increase (higher β values), debris cloud mass increases at a slower rate compared to β because surface mass fluxes are proportional to $v_H^{3/2}$. For increasing β, greater differences are observed between initial and steady-state mean surface mass fluxes, reflecting the negative feedback mechanism associated with the power-law wind speed debris flux relationship.

steady-state surface mass fluxes change proportionally to changes in β (Fig. 1d). For larger β, mean horizontal velocities in the lowest grid layer decrease, resulting in lower steady-state surface mass fluxes compared to the initial value. The reduction in surface mass fluxes is specified by the power-law relationship between wind speed and debris fluxes [i.e., (8)]. For the highest debris loading simulation (β = 16 384), horizontal velocities (raised to the 3/2 power) and steady-state surface mass fluxes are both reduced to 66% of their initial values (Figs. 1c,d).

b. *Axisymmetric debris loading and wind field structure*

To examine debris loading effects in more detail, three simulations are highlighted in which debris loading effects are low (β = 1024), moderate (β = 4096), and high (β = 16 384). Time-averaged, axisymmetric D_L (shown in $\log_{10}$) is shown in Fig. 2 for 0.1-, 0.5-, and 1-mm-radii particles and total D_L for all particles, with β increasing from left to right. These simulations encompass maximum debris loading varying from tenths to a few kilograms per kilogram. For these debris loading scenarios, time-averaged, axisymmetric radial, azimuthal, and vertical velocities and perturbation pressures are shown in Fig. 3. Changes in near-surface winds vary from a few to tens of meters per second.

1) DEBRIS LOADING STRUCTURE

Before discussing the impact of debris loading on tornado dynamics, the axisymmetric spatial structure of debris loading is examined. For each debris loading

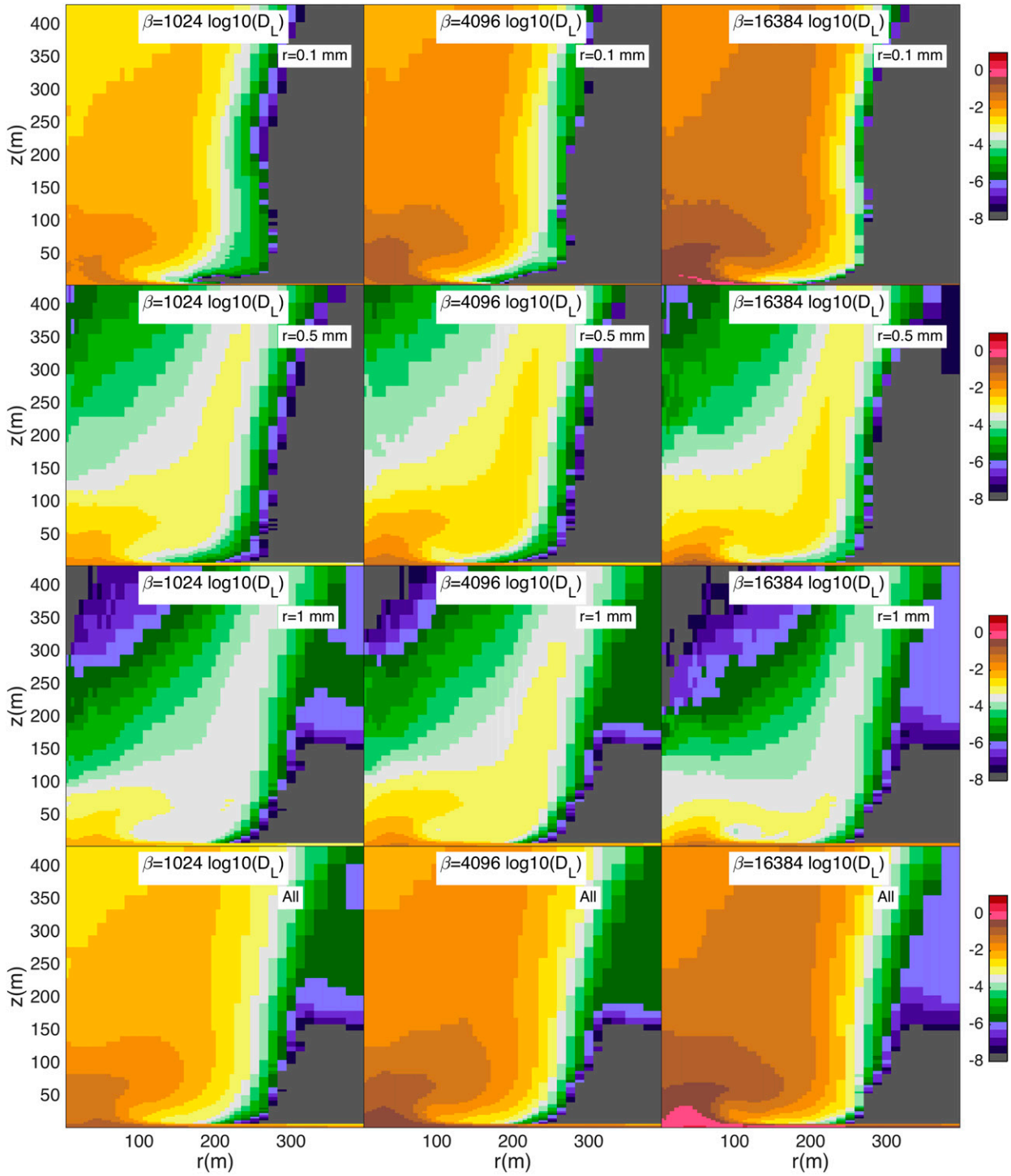

FIG. 2. Mean axisymmetric $\log_{10}$ debris loading for (top)–(bottom) 0.1-, 0.5-, and 1-mm-radii particles and all particles in the r–z plane. (left)–(right) Low, moderate, and high debris loading simulations are shown, corresponding to $\beta = 1024$, 4096, and 16 384.

case, a total D_L maximum occurs within a small annulus where $r < 100$ m and $z < 30$ m AGL (bottom panels in Fig. 2). Within this region, the D_L maximum forms as a result of greater debris lofting within higher vertical velocities and negative radial velocities transporting sand particles from larger radii (Fig. 3). Subvortices also contribute to substantial lofting of debris at these radii, which is discussed further in the next section.

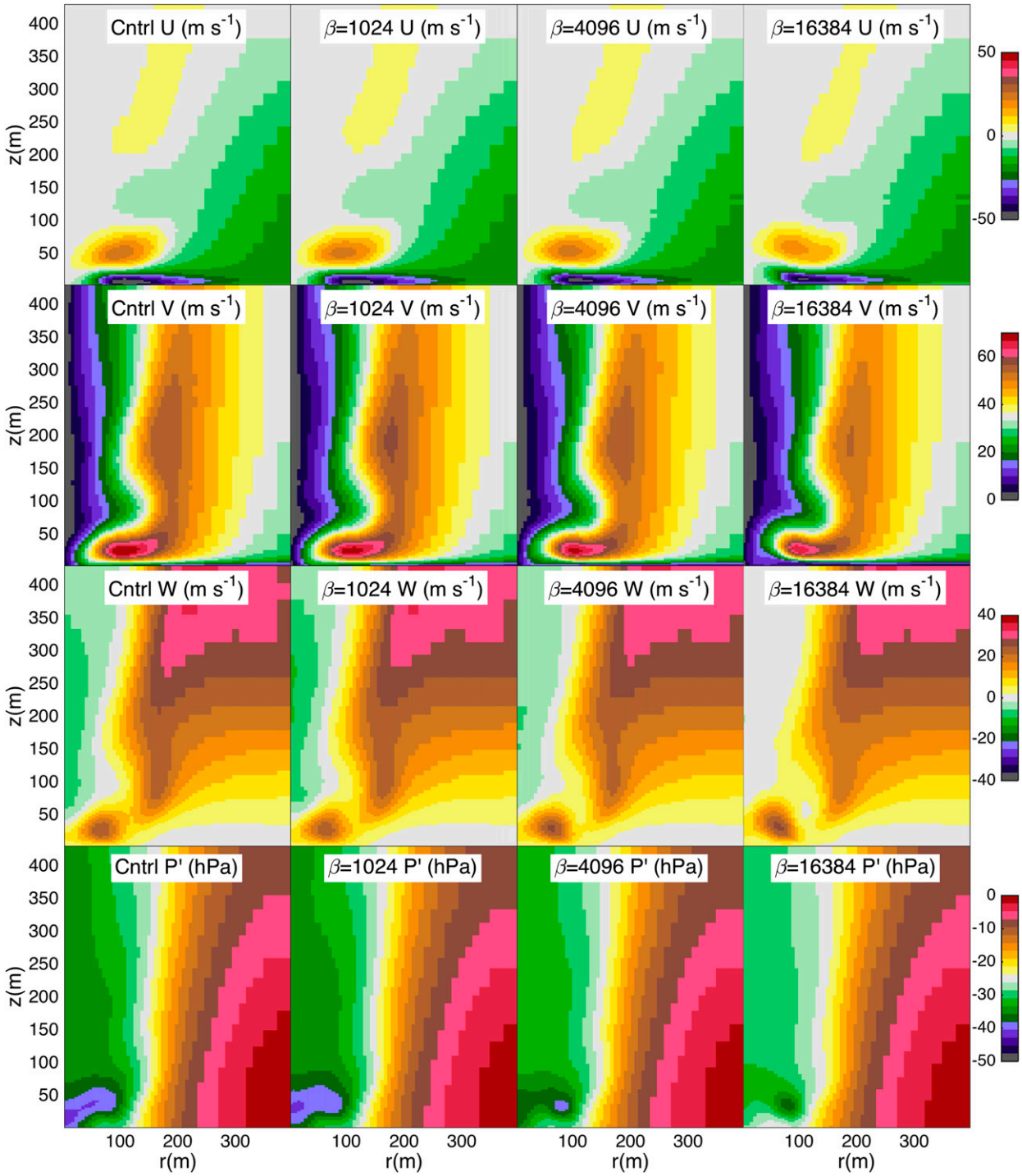

FIG. 3. Mean axisymmetric (top)–(bottom) u, v, w (m s^{-1}), and perturbation pressure p' (hPa) in the r–z plane. (left)–(right) The control simulation and the low, moderate, and high debris loading simulations are shown, corresponding to β = 1024, 4096, and 16 384.

The specified PSD and lofting characteristics of different particle sizes affect the spatial distribution of near-surface debris loading. For the specified PSD, the ratio of the total mass of 0.1-mm-radii particles to the total mass of 1-mm-radii particles is 4.4. Thus, the specified PSD is a contributing factor to higher near-surface D_L of smaller particles. Lofting and centrifuging differences between small and large particles also create differences in near-surface D_L gradients. The greater terminal fall speeds of large particles require stronger

updrafts to be lofted, and centrifugal forces eject large particles faster from favorable lofting regions in updrafts. To examine the change in D_L with height, mean D_L is computed at heights of 10 and 100 m within a 100-m radius for the low ($\beta = 1024$) and high ($\beta = 16\,384$) debris loading simulations. For the low debris loading simulation ($\beta = 1024$) at a height of 100 m compared to 10 m, D_L is smaller by factors of 2.0 and 17.7 for 0.1- and 1-mm-radii particles, respectively (Table 2). As debris loading increases, near-surface vertical velocities also decrease (Fig. 3), causing a larger vertical gradient in mean D_L for both particle sizes. For the high debris loading scenario ($\beta = 16\,384$) at 100 m compared to 10 m, mean D_L is factors of 3.9 and 60.9 smaller for 0.1- and 1-mm-radii particles, respectively (Table 2).

Larger particles move radially outward faster than smaller particles as a consequence of debris centrifuging (Snow 1984; Dowell et al. 2005; Lewellen et al. 2008). Consistent with previous studies, the radius of maximum D_L occurs at greater radii for larger particles and at higher altitudes. Above 200 m AGL, maximum D_L occurs at radii greater than 200 m for 1-mm particles, while maximum D_L is contained within 200 m for 0.1-mm particles (Fig. 2). Within the vortex core, debris centrifuging causes D_L differences of several orders of magnitude between small and large particles for each simulation. For example, 0.1- and 1-mm D_L is $O(10^{-2})$ and $O(10^{-6})\,\mathrm{kg\,kg^{-1}}$, respectively, in the high debris loading simulation at 300 m AGL and $r = 0$ m. Finally, it is noteworthy that, since the sand particle cloud mass is dominated by smaller particles, debris centrifuging does not produce large radial gradients in total D_L for most simulations.

The spatial structure of debris loading exhibits characteristics consistent with frequently observed radar signatures of tornadoes. Debris centrifuging often produces a weak-echo hole (WEH; e.g., Fujita 1981; Wurman et al. 1996; Wurman and Gill 2000; Bluestein and Pazmany 2000; Bluestein et al. 2003; Dowell et al. 2005), characterized by a minimum in radar reflectivity factor surrounded by an annulus of higher reflectivity. Moreover, the radar reflectivity factor is often observed to decrease with height in tornadoes (Wurman et al. 1996; Wurman and Gill 2000; Bluestein et al. 2004; Dowell et al. 2005). At centimeter wavelengths, sand particles are primarily Rayleigh scatterers, and thus radar reflectivity factor increases as a function of d_n^6. In these simulations, radar reflectivity would exhibit a WEH with an increasing radius as a function of height because the radius of the large particle's concentration maxima increases with height. Moreover, a WEH would also be observed in the lowest 50 m AGL. Past studies have suggested that a WEH extending to the surface could provide evidence of a central downdraft (Wurman and Gill 2000). In these simulations, the central downdraft contributes to the low-altitude D_L minimum for larger sand particles within 100 m by inhibiting particle lofting and increasing particle centrifuging through positive radial velocities.

TABLE 2. Mean D_L at 10 and 100 m AGL within a 100-m radius for the low ($\beta = 1024$) and high ($\beta = 16\,384$) debris loading simulation.

β	Height	D_L ($r = 0.1$ mm)	D_L ($r = 1$ mm)
1024	10 m	$0.022\,\mathrm{kg\,kg^{-1}}$	$0.0044\,\mathrm{kg\,kg^{-1}}$
1024	100 m	$0.011\,\mathrm{kg\,kg^{-1}}$	$0.000\,25\,\mathrm{kg\,kg^{-1}}$
16 384	10 m	$0.35\,\mathrm{kg\,kg^{-1}}$	$0.016\,\mathrm{kg\,kg^{-1}}$
16 384	100 m	$0.089\,\mathrm{kg\,kg^{-1}}$	$0.000\,26\,\mathrm{kg\,kg^{-1}}$

2) WIND FIELD STRUCTURE

When axisymmetric mean D_L reaches $0.1\,\mathrm{kg\,kg^{-1}}$ near the surface, debris loading effects on tornado dynamics become evident in axisymmetric mean statistics. Time-averaged, axisymmetric means of minimum radial velocity u, maximum azimuthal velocity v, maximum debris loading, maximum vertical velocity w, and minimum perturbation pressure p' are shown as a function of height for the lowest 100 m AGL in Fig. 4. For simulations with smaller debris loading ($\beta \leq 256$; maximum $D_L < 0.1\,\mathrm{kg\,kg^{-1}}$), maxima and minima statistics of velocity and pressure exhibit similar values to the control simulation. For the $\beta = 1024$ experiment, maximum D_L is $0.11\,\mathrm{kg\,kg^{-1}}$ at $z = 2.7$ m AGL. An increase in minimum u ($3.7\,\mathrm{m\,s^{-1}}$), decrease in maximum v ($3.0\,\mathrm{m\,s^{-1}}$), and increase in p' (2.8 hPa) are observed at $z = 2.7$ m AGL. The impact of debris loading in this simulation, however, is confined to a very small depth, because D_L decreases with height and becomes insufficient to substantially affect tornado wind speeds.

In contrast to lower debris loading experiments in which substantial momentum transfer is confined to a shallow depth and pressure changes are small, the moderate and high debris loading experiments exhibit larger magnitude changes in wind speed and pressure, and these changes occur through a greater depth. For the moderate debris loading experiments ($\beta = 4096$), higher u and p' and lower v and w are observed near the surface (Fig. 3). In the lowest grid cell where maximum D_L is $0.45\,\mathrm{kg\,kg^{-1}}$, maximum v decreases from 26.1 to $16.6\,\mathrm{m\,s^{-1}}$. Debris loading effects are also observed above the corner flow region. The vertical perturbation pressure gradient within a radius of 100 m decreases as a consequence of near-surface v reductions.

Very large changes in wind speeds are observed near the surface in the high debris loading simulation, and

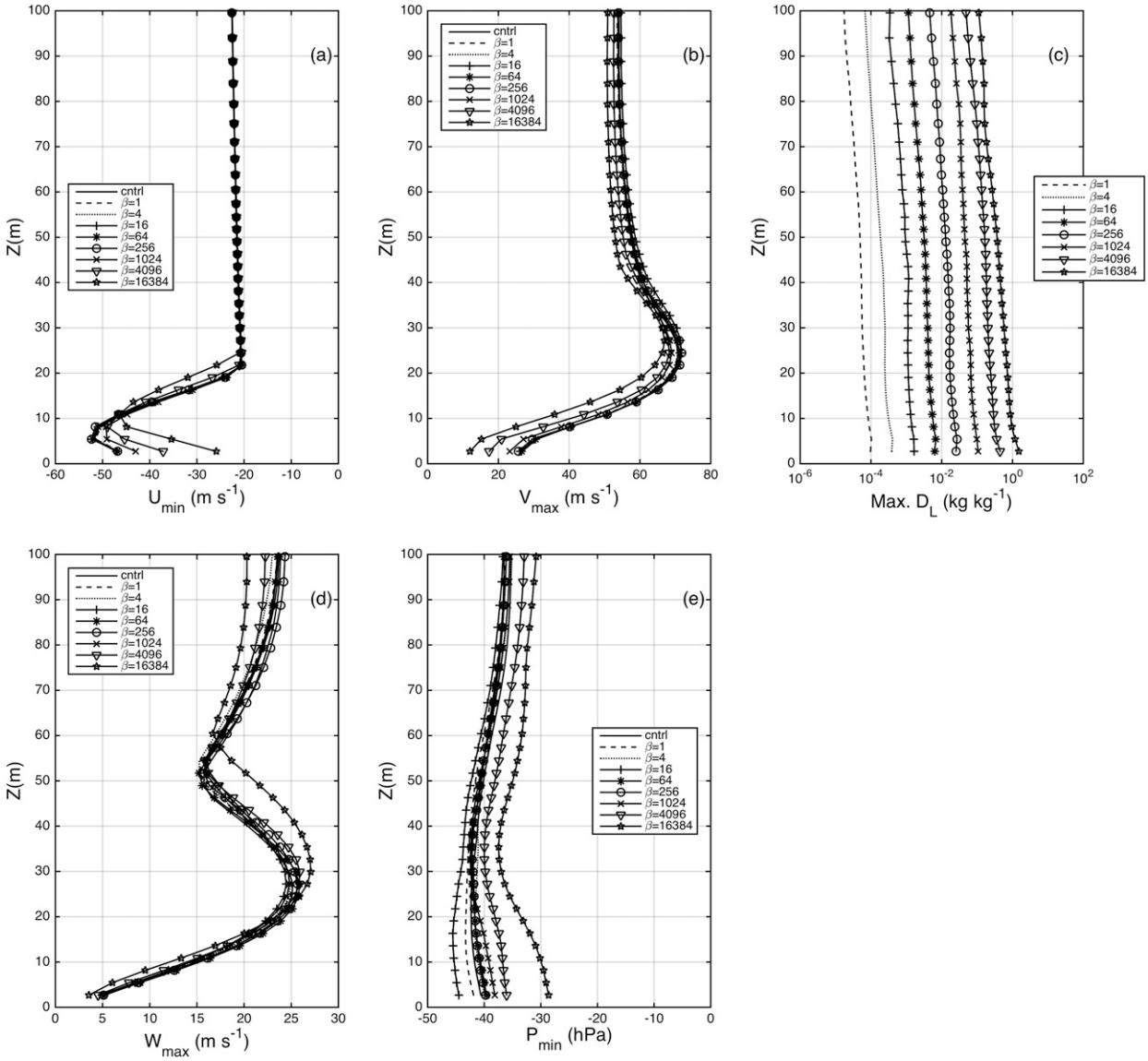

FIG. 4. Time-averaged, steady-state, axisymmetric (a) minimum radial velocity u (m s^{-1}), (b) maximum tangential velocity v (m s^{-1}), (c) maximum debris loading D_L (kg kg^{-1}), (d) maximum vertical velocity w (m s^{-1}), and (e) minimum perturbation pressure p' (hPa) for all debris loading experiments. The maximum and minimum statistics are computed over all radii at each height level.

larger changes are observed aloft. In the high debris loading simulation, domain maximum D_L is 1.5 kg kg^{-1}, and D_L exceeds 0.1 kg kg^{-1} through 105 m AGL. Lowest gridcell minimum u increases by 45% and maximum w decreases by 30%, while lowest gridcell v velocities decrease by 56% (Fig. 4). The reduction in v causes an 11.8-hPa increase in lowest gridcell p'. Maximum and minimum velocities within the domain also exhibit larger changes. Minimum u increases from -51.5 to -46.1 m s^{-1} (10.5%), and maximum v decreases from 70.5 to 66.3 m s^{-1} (5.9%). The change in maximum v for the domain is relatively small, because mean D_L at this location ($r = 93$ m, $z = 27$ m) is less than 0.1 kg kg^{-1}. The D_L maximum of 0.61 kg kg^{-1} at this height occurs at a smaller radius because strong inflow velocities transport sand particles inward. At the radius of D_L maximum ($r = 33$ m, $z = 27$ m), azimuthal velocities are substantially reduced compared to the control simulation. Aloft, a small change in v is observed within the core flow, with maximum v (above 100 m AGL) decreasing from 56.6 to 53.6 m s^{-1}. Finally, maximum w exhibits little change because it occurs at a height of 488 m AGL and debris loading is small [$O(10^{-2})$ kg kg^{-1}].

TABLE 3. Sensitivity tests for the number of trajectories n_t, trajectory time step Δt_{traj}, and minimum vertical resolution $\Delta z_{\min}$ for a high debris loading simulation ($\beta = 16\,384$). Statistics are shown for time-averaged, axisymmetric, steady-state minimum radial velocity $U_{\min}$, maximum azimuthal velocity $V_{\max}$, maximum vertical velocity $W_{\max}$, and minimum pressure $P_{\min}$. Finally, mean spatial pressure variance is computed for 2.7 m AGL $\sigma_p'^2$.

n_t	Δt_{traj} (s)	$\Delta z_{\min}$ (m)	$U_{\min}$ (m s^{-1})	$V_{\max}$ (m s^{-1})	$W_{\max}$ (m s^{-1})	$P_{\min}$ (hPa)	$\sigma_p'^2$ (hPa^2)
11×10^6	0.01	2.7	−46.1	66.4	33.5	−36.9	16.1
22×10^6	0.01	2.7	−46.0	65.6	33.5	−37.0	15.2
5.5×10^6	0.01	2.7	−47.3	67.2	33.2	−38.5	12.7
11×10^6	0.004	2.7	−46.8	66.6	33.4	−37.6	15.5
11×10^6	0.01	3.7	−42.6	63.3	32.9	−33.4	14.3

The debris loading effects on tornado dynamics observed here show similar physical processes to those described in Lewellen et al. (2008). Momentum transfer results in higher u and lower v and w. Since D_L is highest near the surface, the largest momentum transfer occurs here and produces the largest magnitude changes in velocity. Reduced azimuthal velocities increase perturbation pressure in the center of the tornado. As a result, the reduced radial perturbation pressure gradient causes further increases in radial velocities. One interesting difference that we observed is a decrease in minimum w in the lowest 300 m AGL from −8.2 to −2.0 m s^{-1}. We speculate that the reduced vertical perturbation pressure gradient may contribute to the weaker central downdraft.

3) SENSITIVITY TESTS AND INTRAGRIDCELL VELOCITY VARIANCE

Several sensitivity tests were conducted to examine the sensitivity of the results to the simulation configuration, including the number of trajectories, time step, and vertical resolution. Statistics from these tests are presented in Table 3 for the $\beta = 16\,384$ experiment. The largest changes occur between the fine and coarse vertical resolution simulations ($z_{\min} = 2.7$ and 3.7 m), but these changes are less than 10%. Increasing or decreasing the number of trajectories by a factor of 2 has a small effect on maximum and minimum wind speeds and minimum pressure. Finally, decreasing the time step has smallest impact on velocity and pressure statistics, with changes of 2% or less.

Since the current study allows debris velocities to vary within a grid cell, the intragridcell (IGC) variance of debris velocities is examined (i.e., the instantaneous difference between particle velocities in a grid cell). IGC debris velocity variance is shown for 0.1- and 1-mm-radii particles in Fig. 5 for the $\beta = 256$ and 16 384 simulations. Overall, IGC debris velocity variance is quite small, but higher values occur near the surface, where debris loading effects are most substantial. Since the velocities of newly initialized trajectories can differ substantially from the air velocity, a larger IGC variance results as the particles' velocities adjust to the air velocity. Moreover, some particles falling to the surface from aloft have different initial velocities compared to those initialized at the surface. Comparing IGC debris velocity variance for 0.1- and 1-mm-radii particles, the larger particle size has a larger IGC debris velocity variance. Since smaller sand particles have a shorter relaxation time scale (Stackpole 1961; Dowell et al. 2005), they adjust more quickly to the local velocity, which probably minimizes differences between particle trajectories. Debris loading also impacts the IGC debris velocity variance. Compared to the lower debris loading simulation, the high debris loading case exhibits a lower IGC debris velocity variance because velocities and TKE are reduced (TKE discussed in the next section).

c. *Three-dimensional analysis*

In this section, the spatial variability of debris loading is briefly discussed. Then the impact of debris loading on the three-dimensional structure of the tornado wind field is examined with a focus on subvortices.

Subvortices produce complex spatial variability of D_L. For the $\beta = 256$ simulation, an instantaneous cross section of horizontal velocity V_H, w, p', and $\log_{10}$ of D_L are shown in Fig. 6. Two subvortices are evident in the perturbation pressure (Fig. 6c) at the following coordinates: ($X = 30$ m, $Y = -40$ m) and ($X = -30$ m, $Y = -5$ m). Each subvortex has a minimum in D_L in the center surrounded by a ring of higher D_L, similar to WEHs associated with subvortices observed in radar reflectivity data (Wurman and Randall 2001; Wurman et al. 2014; Bluestein et al. 2015). Overall, downdrafts within the radius of maximum wind tend to have lower D_L compared to updraft regions. Additionally, some sand particles are recycled by the downdraft, as observed in Dowell et al. (2005) in their axisymmetric two-cell vortex simulation.

In the control simulation, instantaneous horizontal velocities exceed 120 m s^{-1} (Fig. 7a), which is approximately a factor of 2 greater than mean horizontal velocities in the core flow. Past studies have found that subvortices can exceed mean horizontal velocities in the

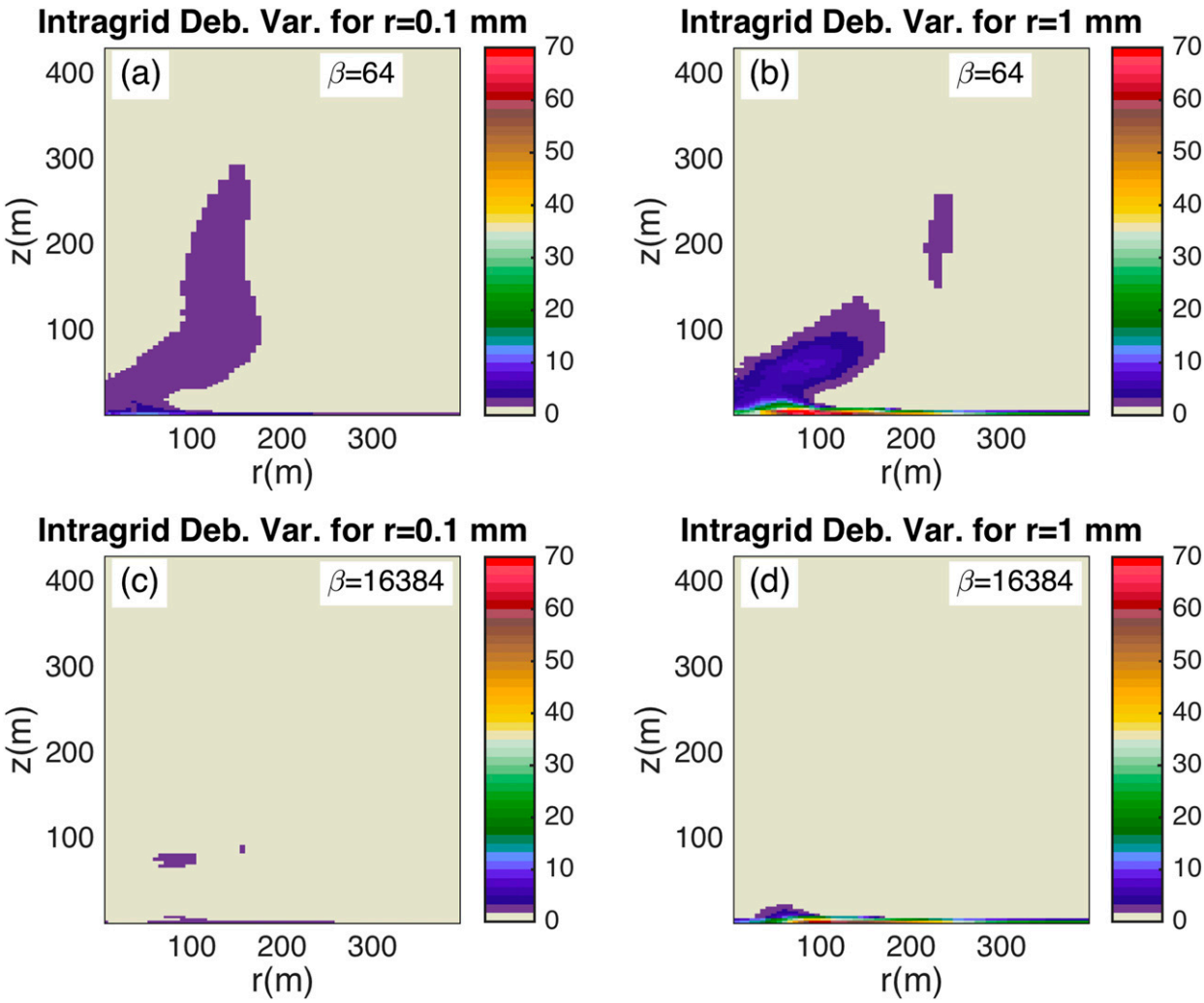

FIG. 5. Axisymmetric mean of intragridcell debris velocity variance ($m^2 s^{-2}$) for 0.1- and 1-mm-radii particles for simulations with $\beta = 256$ and 16 384.

core flow by a factor of 2 (e.g., Fiedler 1998). The subvortices also produce minimum p' as low as -100 hPa (Fig. 7c), which is more than twice the minimum p' for the axisymmetric mean (Fig. 4e).

In the three-dimensional analysis, debris loading effects become evident at smaller β and debris loading compared to the axisymmetric case. Some small reductions in instantaneous maximum V_H and w are observed even at relatively small debris loadings. Thus, although the mean component of the flow remains unaffected, some small amount of debris may act to decrease the turbulent component of the flow and associated maxima. At the higher debris loadings ($\beta = 4096$ and 16 384), maximum V_H and w decrease more substantially. For the high debris loading simulation, maximum V_H and w are reduced by about 60%–70% in the lowest grid cell and by 9% at the altitude of maximum V_H aloft. Maximum total TKE (resolved plus residual) is computed based on Pope (2000, p. 585), and is reduced from 640 to 100 $m^2 s^{-2}$. Compared to the low debris loading simulations, a larger vertical gradient in horizontal wind speed and TKE occurs in the lowest 35 m AGL as a consequence of the large vertical gradient in D_L.

To examine the impact of debris loading on subvortices, statistics are computed based on p'. For these calculations, mean pressure is computed within a 150-m radius to capture the increase in mean pressure caused by debris loading. The mean area where p' is below -15 hPa is shown in Figs. 8a and 8b, and the spatial variance of p' is shown in Figs. 8c and 8d. The largest reduction in mean area occurs at $z = 2.7$ m AGL where p' below -15 hPa are nearly eliminated for the high debris loading simulation. At 13.6 m AGL, mean area decreases by about 38%. The variance of p' also shows similar trends, with

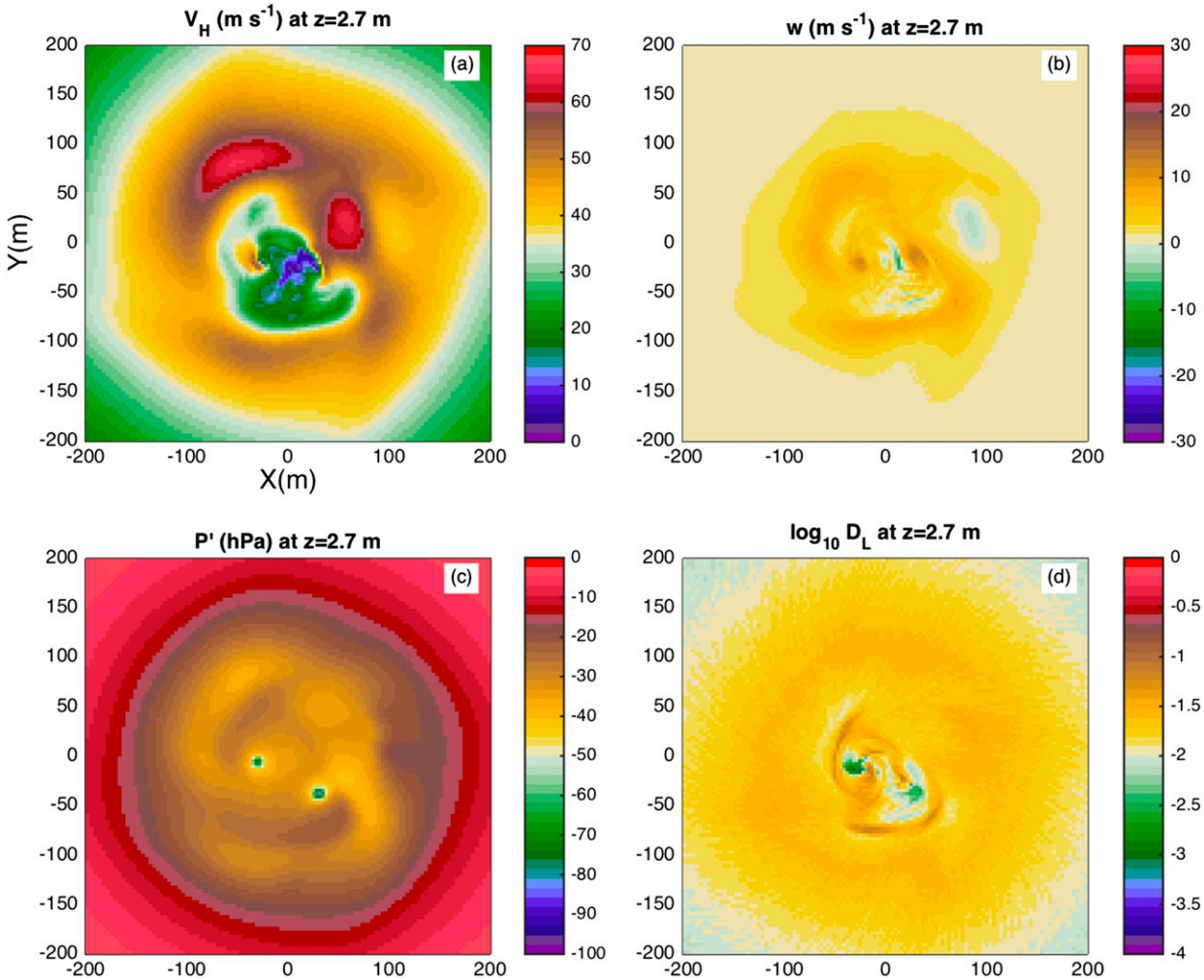

FIG. 6. Instantaneous cross section of (a) horizontal velocity V_H (m s^{-1}), (b) w (m s^{-1}), (c) p' (hPa), and (d) $\log_{10} D_L$ (kg kg^{-1}) for $\beta = 256$ at $z = 2.7$ m AGL. Minima in D_L are collocated with subvortices at ($X = 30$ m, $Y = -40$ m), and ($X = -30$ m, $Y = -5$ m).

the largest decrease in variance occurring near the surface. For subvortices, there are small reductions in p' variance as debris loading increases at 2.7 and 13.6 m AGL as β increases, but the variance begins to decrease rapidly starting with the moderate debris loading scenario. Finally, p' calculations at 2.7 m are shown in Table 3 for different simulation parameters. The largest difference in p' occurs for the case where the number of trajectories is reduced by a factor of 2.

To analyze more detailed characteristics of subvortices, subvortices were identified and tracked manually using the aforementioned perturbation pressure threshold of −15 hPa within a 150-m radius. The positions of these pressure minima are recorded every 1.2 s, and a subvortex number is assigned to pressure minima exhibiting time continuity. For a few cases of merging subvortices, the merged subvortex retains the subvortex number of the more intense subvortex at the previously recorded time. While this analysis is more subjective, it provides a more detailed examination of subvortex characteristics, including subvortex count, duration, pathlength, minimum pressure, and maximum horizontal velocity.

The total number of subvortices, median duration, median pathlength, median minimum pressure, and median maximum horizontal velocity are shown in Fig. 9 for a 115-s period. The most consistent trends occur for the high debris loading simulation. For the high debris loading scenario, the number of subvortices is reduced and median minimum pressure and maximum horizontal velocity decrease at each analysis level (medians computed based on the maximum or minimum value from each subvortex case). At 2.7 m AGL, maximum V_H is reduced by nearly a factor of 2, and subvortices have shorter pathlengths and durations. Moreover, effects on subvortex intensity and pathlength are observed for smaller values of β at $z = 2.7$ m. At the higher analysis heights ($z > 13.6$ m), the

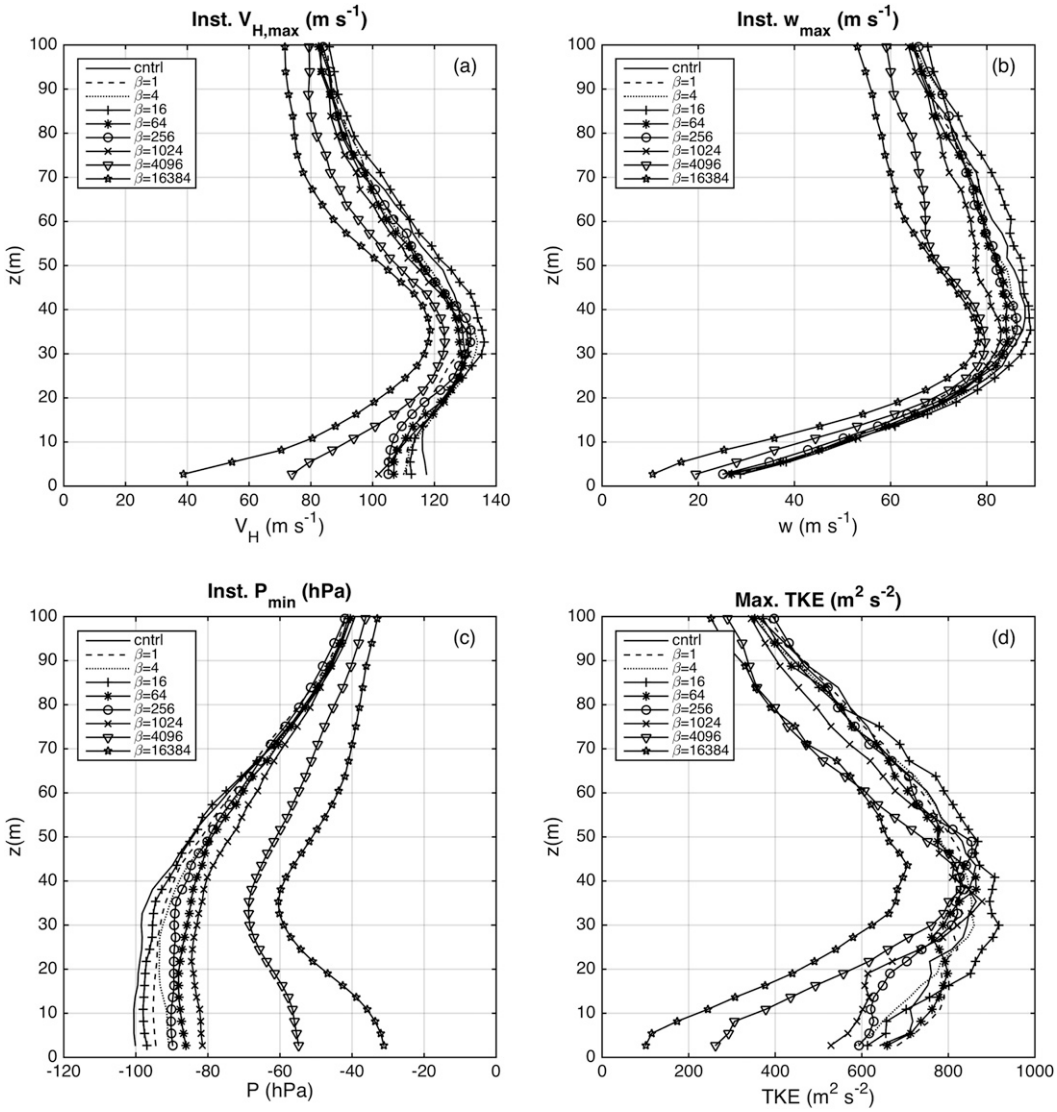

FIG. 7. Time-averaged, three-dimensional (a) instantaneous maximum V_H (m s^{-1}), (b) instantaneous maximum w (m s^{-1}), (c) instantaneous minimum p' (hPa), and (d) maximum total TKE (m^2 s^{-2}).

impact on subvortices becomes less consistent. The most consistent observation is that minimum pressure increases and maximum horizontal velocity decreases for subvortices at some smaller β values (256 and 4096). A consistent trend in pathlength or duration is not observed at higher analysis heights even for higher debris loading (Figs. 9b,c). In contrast to the median statistics for $z >$ 13.6 m, mean pathlength and duration actually increased slightly at moderate and high debris loading because of a few longer-lived subvortices and suppression of shorter-lived ones.

4. Summary and discussion

Debris loading effects on tornado dynamics are simulated using an LES model with two-way drag force coupling between air and sand particles. Particle trajectories are computed for sand-sized particles, with each trajectory representing a number of particles specified by a dynamic scaling factor based on soil PSDs, near-surface wind speeds, and a debris flux factor β. Initial surface mass fluxes are proportional to β, and thus β is varied over several orders of magnitude to encompass the wide variability of surface fluxes expected in nature. Debris loading simulations are conducted for a high-swirl flow with subvortices, and the impact on these subvortices is evaluated.

Debris loading simulations are conducted for a high-swirl ratio case with fixed intensity and zero translation velocity, in addition to fixed debris and aerodynamic parameters (e.g., surface wind speed and debris flux

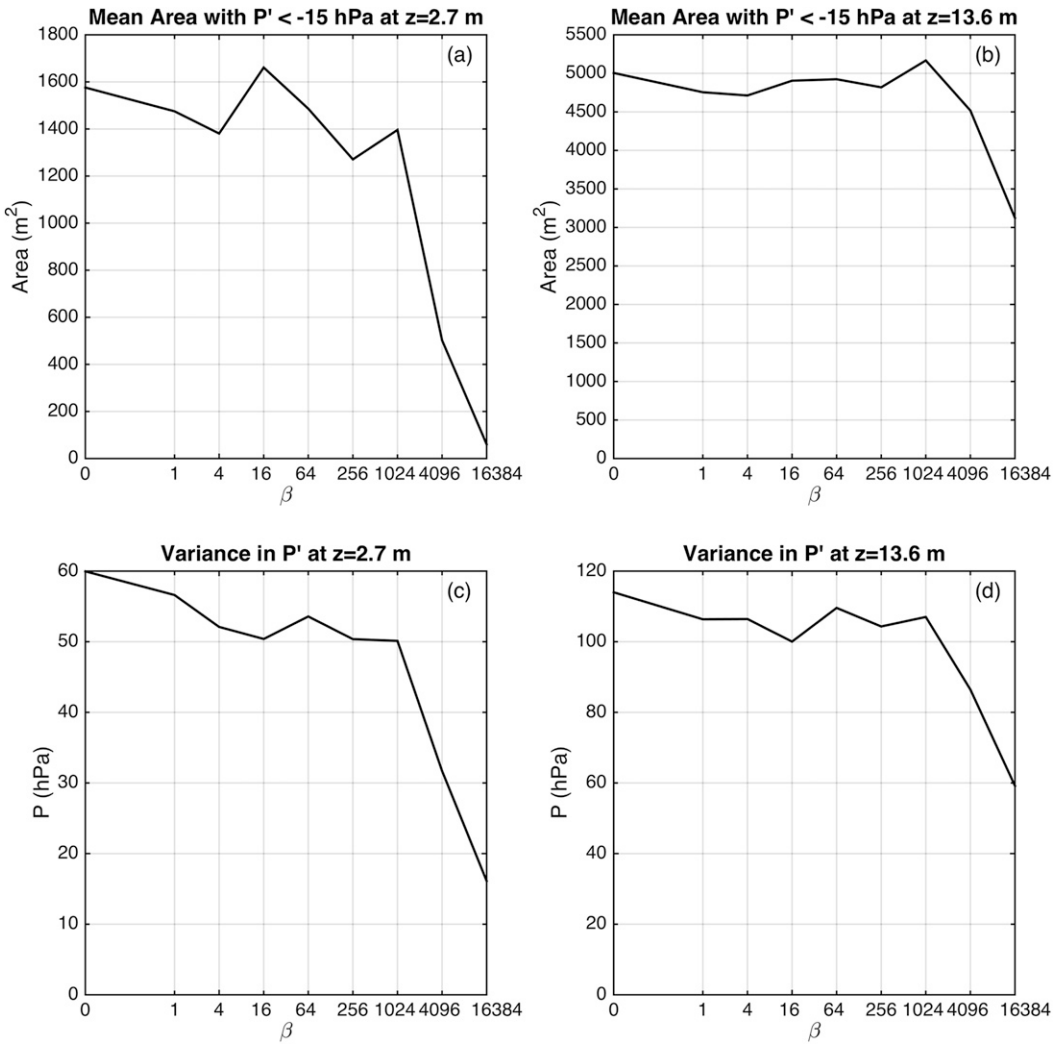

FIG. 8. (top) Mean area (m^2), where p' (mean pressure computed within a 150-m radius) is below -15 hPa at (a) 2.7 and (b) 13.6 m AGL, and (bottom) variance of p' (hPa^2) at (c) 2.7 and (d) 13.6 m AGL. For the high debris loading scenario, the low perturbation pressure area is nearly eliminated at 2.7 m and reduced by a factor of 2 at 13.6 m. The variance of p' also shows similar characteristics with increasing debris loading, decreasing by a factor of approximately 3 and 2 at heights of 2.7 and 13.6 m.

relationship). Thus, it is stressed that these conclusions apply to this specific case, and its applicability to debris loading effects on tornado dynamics for different sets of these parameters remains untested. For the case examined herein, β sensitivity tests produce mean lowest grid layer debris fluxes ranging from about 10^{-4} to about $1\,\mathrm{kg\,m^{-2}\,s^{-1}}$ and total debris cloud masses from 10^3 to 10^7 kg. Simulations by Lewellen et al. (2008) with smaller-radii particles also produced debris clouds $O(10^7)$ kg. The negative feedback mechanism discussed in Lewellen et al. (2008), for which increasing initial surface mass fluxes result in lower velocities and thereby reduce time-averaged debris fluxes, was also examined. Time-averaged debris cloud mass increases by only 42% of the tested β range. For comparison, Lewellen et al. (2008) found a 20% change in debris cloud mass at high debris loading when surface fluxes were varied by a factor of 2. For small β (surface mass fluxes $< 10^{-2}\,\mathrm{kg\,m^{-2}\,s^{-1}}$), the negative feedback mechanism has little impact because near-surface velocities remain relatively unchanged. However, as β increases, debris loading reduces wind speeds, which reduces time-averaged surface mass fluxes through the specified power-law relationship between wind speed and scaling factor.

While the specified soil PSD has some impact on the spatial distributions of D_L for different particle radii, D_L differences between small and large particles increase as height increases. Smaller particles are more easily lofted

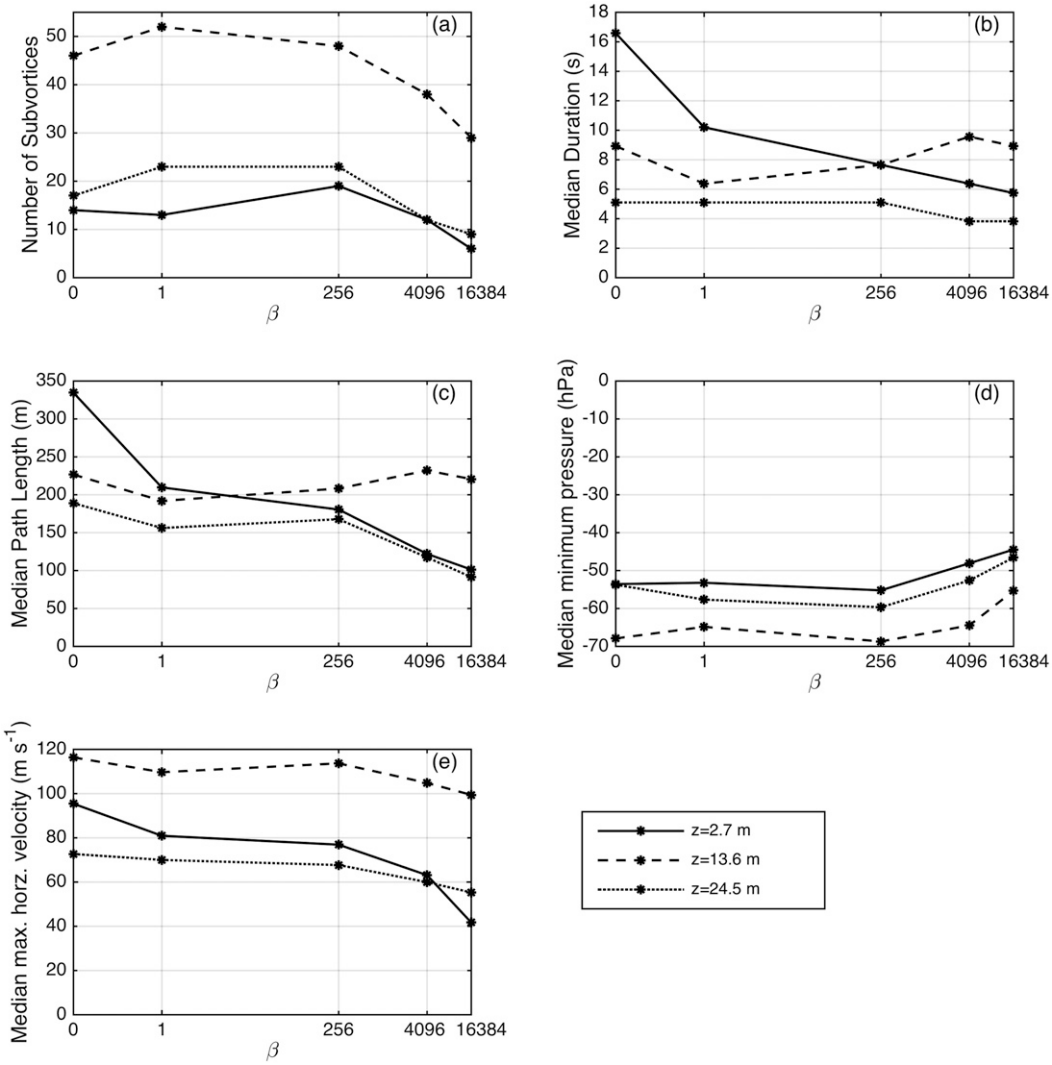

FIG. 9. Subvortex characteristics from manual tracking using a perturbation pressure threshold of -15 hPa, including (a) number of subvortices, and median (b) duration (s), (c) pathlength (m), (d) minimum pressure (hPa), and (e) maximum horizontal velocity (m s^{-1}). Analyses are shown for the control simulation ($\beta = 0$), and $\beta = 1, 256$, 4096, and 16 384.

and are centrifuged from updrafts more slowly compared to larger particles. As a result, D_L for larger particles decreases faster with height. In the vortex core aloft, differences in D_L between large and small particles can be several orders of magnitude as a consequence of debris centrifuging and fallout of larger particles. Decreasing particle concentrations and sizes with height have been inferred from radar observations (Wurman et al. 1996; Wurman and Gill 2000; Bluestein et al. 2004; Dowell et al. 2005) and numerical simulations (Dowell et al. 2005; Lewellen et al. 2008). Radial gradients in D_L are observed extending to the surface and would likely produce a WEH extending down to the surface. A WEH extending to the surface has been attributed to downdrafts in past studies (Wurman and Gill 2000).

As surface debris fluxes and debris loading increase, the following impacts on the mean flow of this high-swirl flow occur. Debris loading effects on the high-swirl flow are observed on the mean flow once maximum $D_L \geq 0.1\,\mathrm{kg\,kg^{-1}}$ and surface debris fluxes are $\geq 10^{-2}\,\mathrm{kg\,m^{-2}\,s^{-1}}$. At D_L of $0.1\,\mathrm{kg\,kg^{-1}}$, horizontal wind speeds change by a few meters per second or less in the lowest grid cell as a result of momentum transfer. As debris loading increases toward a maximum D_L of $1\,\mathrm{kg\,kg^{-1}}$ or greater, debris loading effects occur through a greater depth, and larger magnitude changes are observed near the surface. In addition to larger momentum transfer

over a greater depth, greater reductions in azimuthal velocity produce an increase in perturbation pressure, as observed in Lewellen et al. (2008). For the high debris loading scenario, axisymmetric means of maximum horizontal velocity are reduced by up to 55% in the lowest 10 m AGL, and a 6% reduction is observed at the altitude of maximum wind.

Debris loading effects on turbulent characteristics of tornado dynamics exhibit some similarities and differences compared to the mean characteristics. For the moderate to high debris loading cases, instantaneous maximum horizontal velocities are reduced by similar percentages as axisymmetric means of maximum horizontal velocities. Maximum TKE is also reduced by up to 70%–85% in the lowest 10 m AGL. However, small effects on maximum horizontal velocities and TKE are evident at debris loading levels as small as 0.01 $\mathrm{kg\,kg^{-1}}$. Thus, debris loading effects on turbulent characteristics of the flow may occur at smaller levels of debris loading.

In the control simulation, subvortices permit instantaneous maximum horizontal velocities to exceed mean velocities aloft by a factor of 2. The impact on subvortices was quantified by tracking individual subvortices and computing areas of thresholded pressure minima and spatial pressure variance. At moderate and high debris loading, spatial pressure variance, the number of subvortices, and subvortex maximum intensity decrease compared to the control simulations. At 2.7 m AGL, subvortex intensity decreased at smaller β values, consistent with the debris loading effects observed with the analysis of instantaneous maximum velocities and TKE. Also, the pathlength and duration of subvortices is reduced significantly. At higher altitudes, however, subvortex intensity is reduced, while the impact on pathlength and duration remains unclear. Simulations by Gong (2006) and Lewellen et al. (2008) also note that, at high debris loading, subvortices can be reduced or eliminated. In the present study, subvortices appear to be inhibited at moderate to high debris loading, but the impact on subvortices at small debris loadings is less substantial. Since large azimuthal and vertical velocity gradients are needed for subvortex formation (e.g., Rotunno 1978; Gall 1983; Lewellen et al. 2000; Nolan 2012), reduced azimuthal and vertical velocity gradients near the surface may be a contributing factor to a reduction in the number of subvortices.

This study examined specific cases with a high-swirl ratio flow in which surface debris fluxes were varied while the soil PSD and relationship between wind speed and debris fluxes remained constant. As a result, a more extensive study is needed to examine the applicability of these findings to different flow characteristics (swirl ratios, intensities, and translation velocities) and surface debris properties (e.g., PSD, debris depth, wind speed, and debris flux relationship). For a lower-swirl ratio case, the smaller core diameter and enhanced centrifuging could lead to smaller debris loading. Lewellen et al. (2008) found that corner flow swirl ratio (S_c; Lewellen et al. 2000; Lewellen and Lewellen 2007a) increased at high debris loading because near-surface radial wind speeds decreased more than azimuthal wind speeds, and thus additional feedbacks may occur as a consequence of swirl ratio changes. Moreover, the heights of near-surface radial and azimuthal wind maxima vary as a function of swirl ratio, and thus more elevated wind speed maxima may generate lower debris loading. Since larger particles tend to be centrifuged and fall out faster, soil PSDs with larger (smaller) particle sizes may have smaller (larger) debris loading effects. Finally, since surface and tornado flow characteristics change throughout a tornado's lifetime, future studies should examine how variations in tornado flow or surface characteristics affect debris loading impacts on tornado dynamics.

The possibility of substantial changes in tornado dynamics necessitates an observational examination of debris loading effects and assessment of relationships between surface debris fluxes and wind characteristics. While Doppler radars provide some qualitative information about particle sizes and concentrations in addition to Doppler velocity, quantitative information about debris characteristics has not been obtained. Nonetheless, radar simulations of tornado debris clouds with sand particles and other scatterers may be useful to assess the feasibility of using radar measurements to estimate debris loading. A detailed electromagnetic characterization of soil particles is needed to understand how different soil characteristics affect radar signatures (e.g., wetness and complex relative permittivity). Lidar observations (Bluestein et al. 2014) may also help examine surface debris flux relationships to wind speed in tornadic inflow regions since lidar observations can be obtained closer to the surface compared to radars. The present simulation work will continue to examine a greater range of debris types. Future numerical simulations could examine debris loading effects of large particles on tornado wind speeds. The two-way drag force feedback model developed in this study can be extended to nonspherical debris (e.g., "2×4s" or roof tiles) using a 6-degree-of-freedom model (Richards et al. 2008; Maruyama and Noda 2012), which allows drag and moment coefficients to vary as a function of orientation. Although a substantial portion of large tornado-generated debris may not be lofted to high altitudes (Magsig and Snow 1998; Dowell et al. 2005), debris may reside within the corner flow for a sufficiently long period to affect tornado dynamics.

Acknowledgments. This study is based upon work supported by the National Science Foundation under Grants AGS-1303685 and OISE-1209444. The first author is supported by the National Center for Atmospheric Research (NCAR) Advanced Study Program. H. Bluestein is supported by NSF Grant AGS-1262048. The authors also acknowledge the Collaborative Research program of Joint Usage/Collaborative Research Center for Multidisciplinary Disaster Prevention Study: DPRI Kyoto University. The authors greatly appreciate reviews of the manuscript from Dave Lewellen and two anonymous reviewers, which have helped improve the study. Discussions with George Bryan and Rich Rotunno on boundary conditions helped improve the numerical simulations. The authors appreciate comments from George Bryan and Jim Wilson on an early draft of the manuscript.

REFERENCES

Anderson, R. S., and P. K. Haff, 1991: Wind modification and bed response during saltation of sand in air. *Aeolian Grain Transport 1*, O. E. Barndorff-Nielsen and B. B. Willetts, Eds., Acta Mechanica Supplementum, Vol. 1, Springer Vienna, 21–51, doi:10.1007/978-3-7091-6706-9_2.

Batt, R. G., M. P. Petach, S. A. Peabody II, and R. R. Batt, 1999: Boundary layer entrainment of sand-sized particles at high speed. *J. Fluid Mech.*, **392**, 335–360, doi:10.1017/S0022112099005510.

Bluestein, H. B., and A. L. Pazmany, 2000: Observations of tornadoes and other convective phenomena with a mobile, 3-mm wavelength, Doppler radar: The spring 1999 field experiment. *Bull. Amer. Meteor. Soc.*, **81**, 2939–2951, doi:10.1175/1520-0477(2000)081<2939:OOTAOC>2.3.CO;2.

——, W.-C. Lee, M. Bell, C. C. Weiss, and A. L. Pazmany, 2003: Mobile Doppler radar observations of a tornado in a supercell near Bassett, Nebraska, on 5 June 1999. Part II: Tornado-vortex structure. *Mon. Wea. Rev.*, **131**, 2968–2984, doi:10.1175/1520-0493(2003)131<2968:MDROOA>2.0.CO;2.

——, C. C. Weiss, and A. L. Pazmany, 2004: The vertical structure of a tornado near Happy, Texas, on 5 May 2002: High-resolution, mobile, W-band, Doppler radar observations. *Mon. Wea. Rev.*, **132**, 2325–2337, doi:10.1175/1520-0493(2004)132<2325:TVSOAT>2.0.CO;2.

——, J. Houser, M. French, J. Snyder, G. Emmitt, I. PopStefanija, C. Baldi, and R. Bluth, 2014: Observations of the boundary layer near tornadoes and in supercells using a mobile, co-located, pulsed Doppler lidar and radar. *J. Atmos. Oceanic Technol.*, **31**, 302–325, doi:10.1175/JTECH-D-13-00112.1.

——, J. C. Snyder, and J. B. Houser, 2015: A multiscale overview of the El Reno, Oklahoma, tornadic supercell of 31 May 2013. *Wea. Forecasting*, **30**, 525–552, doi:10.1175/WAF-D-14-00152.1.

Bodine, D., M. R. Kumjian, R. D. Palmer, P. L. Heinselman, and A. V. Ryzhkov, 2013: Tornado damage estimation using polarimetric radar. *Wea. Forecasting*, **28**, 139–158, doi:10.1175/WAF-D-11-00158.1.

Dowell, D. C., C. R. Alexander, J. M. Wurman, and L. J. Wicker, 2005: Centrifuging of hydrometeors and debris in tornadoes: Radar-reflectivity patterns and wind-measurement errors. *Mon. Wea. Rev.*, **133**, 1501–1524, doi:10.1175/MWR2934.1.

Fiedler, B. H., 1998: Wind-speed limits in numerically simulated tornadoes with suction vortices. *Quart. J. Roy. Meteor. Soc.*, **124**, 2377–2392, doi:10.1002/qj.49712455110.

Fujita, T. T., 1981: Tornadoes and downbursts in the context of generalized planetary scales. *J. Atmos. Sci.*, **38**, 1511–1534, doi:10.1175/1520-0469(1981)038<1511:TADITC>2.0.CO;2.

Gall, R. L., 1983: A linear analysis of the multiple vortex phenomenon in simulated tornadoes. *J. Atmos. Sci.*, **40**, 2010–2024, doi:10.1175/1520-0469(1983)040<2010:ALAOTM>2.0.CO;2.

Gong, B., 2006: Large-eddy simulation of the effects of debris on tornado dynamics. Ph.D. thesis, West Virginia University, 187 pp.

Huang, N., G. Yue, and X. Zheng, 2008: Numerical simulation of a dust devil and the electric field in it. *J. Geophys. Res.*, **113**, D20203, doi:10.1029/2008JD010182.

Lewellen, D. C., and W. S. Lewellen, 2007a: Near-surface intensification of tornado vortices. *J. Atmos. Sci.*, **64**, 2176–2194, doi:10.1175/JAS3965.1.

——, and ——, 2007b: Near-surface vortex intensification through corner flow collapse. *J. Atmos. Sci.*, **64**, 2195–2209, doi:10.1175/JAS3966.1.

——, ——, and J. Xia, 2000: The influence of a local swirl ratio on tornado intensification near the surface. *J. Atmos. Sci.*, **57**, 527–544, doi:10.1175/1520-0469(2000)057<0527:TIOALS>2.0.CO;2.

——, B. Gong, and W. S. Lewellen, 2004: Effects of debris on near-surface tornado dynamics. *22nd Conf. on Severe Local Storms*, Hyannis, MA, Amer. Meteor. Soc., 15.5. [Available online at https://ams.confex.com/ams/11aram22sls/techprogram/paper_81449.htm.]

——, ——, and ——, 2008: Effects of finescale debris on near-surface tornado dynamics. *J. Atmos. Sci.*, **65**, 3247–3262, doi:10.1175/2008JAS2686.1.

Lewellen, W. S., D. C. Lewellen, and R. I. Sykes, 1997: Large-eddy simulation of a tornado's interaction with the surface. *J. Atmos. Sci.*, **54**, 581–605, doi:10.1175/1520-0469(1997)054<0581:LESOAT>2.0.CO;2.

Magsig, M. A., and J. T. Snow, 1998: Long-distance debris transport by tornadic thunderstorms. Part I: The 7 May 1995 supercell thunderstorm. *Mon. Wea. Rev.*, **126**, 1430–1449, doi:10.1175/1520-0493(1998)126<1430:LDDTBT>2.0.CO;2.

Maruyama, T., 2011: Simulation of flying debris using a numerically generated tornado-like vortex. *J. Wind Eng. Ind. Aerodyn.*, **99**, 249–256, doi:10.1016/j.jweia.2011.01.016.

——, and M. Noda, 2012: Tornado-borne debris. *J. Appl. Wind Eng.*, **37**, 124–129, doi:10.5359/jawe.37.124.

Metzger, S. M., M. R. Balme, M. C. Towner, B. J. Bos, T. J. Ringrose, and M. R. Patel, 2011: In situ measurements of particle load and transport in dust devils. *Icarus*, **214**, 766–772, doi:10.1016/j.icarus.2011.03.013.

Neakrase, L. D. V., and R. Greeley, 2010: Dust devils in the laboratory: Effect of surface roughness on vortex dynamics. *J. Geophys. Res.*, **115**, E05003, doi:10.1029/2009JE003465.

Nolan, D. S., 2012: Three-dimensional instabilities in tornado-like vortices with secondary circulations. *J. Fluid Mech.*, **711**, 61–100, doi:10.1017/jfm.2012.369.

Pope, S. B., 2000: *Turbulent Flows*. University Press, 802 pp.

Richards, P. J., N. Williams, B. Laing, M. McCarty, and M. Pond, 2008: Numerical calculation of the three-dimensional motion of wind-borne debris. *J. Wind Eng. Ind. Aerodyn.*, **96**, 2188–2202, doi:10.1016/j.jweia.2008.02.060.

Rotunno, R., 1978: A note on the stability of a cylindrical vortex sheet. *J. Fluid Mech.*, **87**, 761–771, doi:10.1017/S0022112078001871.

Ryzhkov, A. V., D. Burgess, D. Zrnić, T. Smith, and S. Giangrande, 2002: Polarimetric analysis of a 3 May 1999 tornado. *21st Conf. on Severe Local Storms*, San Antonio, TX, Amer. Meteor. Soc., 14.2. [Available online at https://ams.confex.com/ams/SLS_WAF_NWP/techprogram/paper_47348.htm.]

——, T. J. Schuur, D. W. Burgess, and D. S. Zrnić, 2005: Polarimetric tornado detection. *J. Appl. Meteor.*, **44**, 557–570, doi:10.1175/JAM2235.1.

Schultz, C. J., and Coauthors, 2012: Dual-polarization tornadic debris signatures. Part II: Comparisons and caveats. *Electron. J. Oper. Meteor.*, **13**, 138–158.

Smagorinsky, J., 1963: General circulation experiments with the primitive equations. I: The basic experiment. *Mon. Wea. Rev.*, **91**, 99–162, doi:10.1175/1520-0493(1963)091<0099:GCEWTP>2.3.CO;2.

Snow, J. T., 1984: On the formation of particle sheaths in columnar vortices. *J. Atmos. Sci.*, **41**, 2477–2491, doi:10.1175/1520-0469(1984)041<2477:OTFOPS>2.0.CO;2.

Stackpole, J. D., 1961: The effectiveness of raindrops as turbulence sensors. Preprints, *Ninth Weather Radar Conf.*, Kansas City, MO, Amer. Meteor. Soc., 212–217.

Turcotte, D. L., 1986: Fractals and fragmentation. *J. Geophys. Res.*, **91**, 1921–1926, doi:10.1029/JB091iB02p01921.

Tyler, S. W., and S. W. Wheatcraft, 1989: Application of fractal mathematics to soil water retention estimation. *Soil. Sci. Soc. Amer. J.*, **53**, 987–995, doi:10.2136/sssaj1989.03615995005300040001x.

——, and ——, 1992: Fractal scaling of soil particle-size distributions: Analysis and limitations. *Soil. Sci. Soc. Amer. J.*, **56**, 362–369, doi:10.2136/sssaj1992.03615995005600020005x.

Uchida, T., and Y. Ohya, 2003: Large-eddy simulation of turbulent airflow over complex terrain. *J. Wind Eng. Ind. Aerodyn.*, **91**, 219–229, doi:10.1016/S0167-6105(02)00347-1.

Van Den Broeke, M. S., and S. T. Jauernic, 2014: Spatial and temporal characteristics of polarimetric tornadic debris signatures. *J. Appl. Meteor. Climatol.*, **53**, 2217–2231, doi:10.1175/JAMC-D-14-0094.1.

White, F. M., 1991: *Viscous Fluid Flow*. McGraw-Hill, 614 pp.

Wurman, J., and S. Gill, 2000: Finescale radar observations of the Dimmitt, Texas (2 June 1995), tornado. *Mon. Wea. Rev.*, **128**, 2135–2164, doi:10.1175/1520-0493(2000)128<2135:FROOTD>2.0.CO;2.

——, and M. Randall, 2001: An inexpensive, mobile, rapid-scan radar. *Extended Abstracts, 30th Int. Conf. on Radar Meteorology*, Munich, Germany, Amer. Meteor. Soc., P3.4. [Available online at https://ams.confex.com/ams/30radar/techprogram/paper_21577.htm.]

——, J. M. Straka, and E. N. Rasmussen, 1996: Fine-scale Doppler radar observations of tornadoes. *Science*, **272**, 1774–1777, doi:10.1126/science.272.5269.1774.

——, K. Kosbia, P. Robinson, and T. Marshall, 2014: The role of multiple-vortex tornado structure in causing storm researcher fatalities. *Bull. Amer. Meteor. Soc.*, **95**, 31–45, doi:10.1175/BAMS-D-13-00221.1.